



Cite this: *RSC Adv.*, 2022, 12, 20481

Preparation and photodynamic antibacterial/anticancer effects of ultralong-lifetime room-temperature phosphorescent N-doped carbon dots†

Yanming Miao, * Xinhao Zhang, Jinyao Li, Wenli Yang, Xiaomin Huang and Jinzhi Lv*

Room-temperature phosphorescent (RTP) N-doped carbon-dots (CNDs) featuring eco-friendliness, low cost and high biocompatibility, are ideal photodynamic antibacterial and anticancer nanomaterials. However, the existing CNDs are limited by low singlet oxygen ($^1\text{O}_2$) quantum yield, which has become a bottleneck in the development of CNDs. One basic reason is the short T_1 -state exciton lifetime of CNDs. Herein, triethylenetetramine hexaacetic acid was used to synthesize CNDs *via* a one-step hydrothermal method. CNDs are characterized with low toxicity, high biocompatibility and ultralong-lifetime RTP (URTP). In addition to the URTP (average lifetime 414 ms) under solid conditions, CNDs even had URTP (average lifetime 320 ms) in a water environment. The ultralong T_1 exciton lifetime largely extends the collision time between T_1 state excitons and O_2 and prolongs the energy transfer time, not only improving the quantum yield (0.63) of singlet oxygen ($^1\text{O}_2$) in solution, but also facilitating the photodynamic antibacterial and anticancer effects.

Received 8th April 2022
Accepted 9th June 2022

DOI: 10.1039/d2ra02251f

rsc.li/rsc-advances

Introduction

Photodynamic antibacterial and anticancer effects based on photosensitizers are considered as effective antibacterial and anticancer replacement therapies with few side effects, which can be rapidly and repeatedly used.^{1,2} Given the easy production and high oxidation activity, $^1\text{O}_2$ is the core molecule of the photodynamic effect, and oxygen (O_2) is the most abundant, cheapest and green oxidizer and the main source of $^1\text{O}_2$ generation. However, since O_2 has a triplet state ($^3\text{O}_2$, spin prohibition) and dynamic stability, a photosensitizer is usually needed to overcome spin prohibition before the triplet state oxygen ($^3\text{O}_2$) can be converted to the singlet state ($^1\text{O}_2$). Nevertheless, the commonly-used photosensitizers including various organic dyes^{3,4} and nanomaterials (*e.g.* graphene quantum dots,⁵ black phosphorus,⁶ graphite carbon nitride,⁷ metal organic frameworks⁸) are limited by low photosensitivity, which results in low $^1\text{O}_2$ quantum yield, or low water solubility and biocompatibility, or complex synthetic conditions. This limitation restricts their photodynamic antibacterial and anticancer applications. Hence, novel photosensitizers should be developed to improve $^1\text{O}_2$ quantum yields. Room-temperature

phosphorescent (RTP) photosensitizers create a new route to solve the above problem.

Room-temperature phosphorescence (RTP) is caused by a triplet excited state (T_1) transition,^{9–11} so RTP photosensitizers have very large T_1 exciton quantum yields. Since the ground state of O_2 molecules is a triplet state, RTP photosensitizers, through the energy transfer between T_1 excitons and O_2 molecules, generate more highly-oxidizing $^1\text{O}_2$.^{9,12} Moreover, since energy transfer is achieved through intermolecular collision, for a photosensitizer with longer RTP lifetime (longer T_1 exciton lifetime), the probability of collision and energy transfer between O_2 molecules is higher, the photosensitizer is more sensitive to O_2 , and the $^1\text{O}_2$ quantum yield is larger. Hence, ultralong-lifetime RTP (URTP) photosensitizers have higher $^1\text{O}_2$ yields.^{13,14} Thus, one key factor in improving $^1\text{O}_2$ quantum yields is to prepare RTP photosensitizers with long-lifetime T_1 -state excitons.

As novel photoluminescent nanomaterials, carbon dots (CDs) feature simple preparation, low cost, low toxicity and high biocompatibility, and are extensively applied in photoelectric devices,^{15,16} sensors,^{17,18} catalysis,^{19,20} bacterial therapy,^{21,22} and forgery prevention.^{23,24} Specifically, N-doped carbon dot (CND) RTP nanomaterials have higher T_1 quantum yield, and more easily convert the ground state triplet O_2 to $^1\text{O}_2$, and CNDs have the characteristics of low cost and high biocompatibility. Therefore, CNDs are ideal materials for photodynamic bacteria and cancer applications. However, the $^1\text{O}_2$ quantum yield of CNDs is still relatively low, which is mainly due to the short RTP

School of Life Science, Shanxi Normal University, Taiyuan 030006, PR China. E-mail: mym8207@126.com; lvjinzhi208@126.com; Tel: +86-0351-2051196

† Electronic supplementary information (ESI) available. See <https://doi.org/10.1039/d2ra02251f>



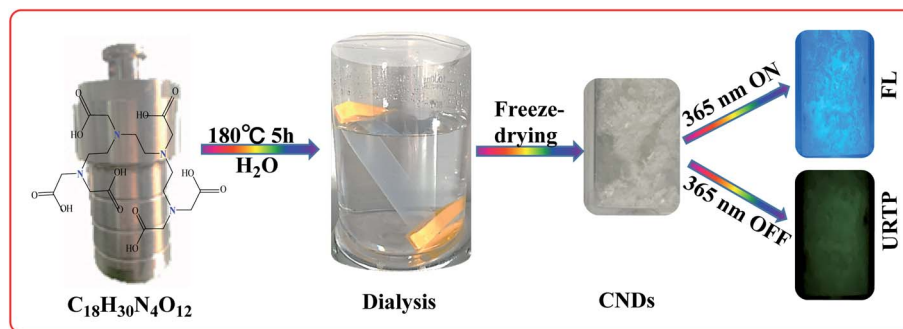


Fig. 1 Schematic diagram of the preparation of CNDs.

lifetime of the commonly synthesized CND materials and the short collision time between T_1 state excitons and O_2 , resulting in a short energy transfer time, which has become the bottleneck of their development.

In this study, CNDs were synthesized from triethylenetetramine hexaacetic acid (TTHA) *via* a one-step hydrothermal method. Although some researchers have synthesized fluorescent CDs with triethylenetetramine hexaacetic acid in alkaline aqueous solution and at 250 °C,²⁵ in this study, CNDs were synthesized with triethylenetetramine hexaacetic acid in pure water and at a lower temperature (180 °C), and the synthesized CNDs have URTP properties. The CNDs not only have low toxicity and good biocompatibility, but also have URTP properties. The ultralong T_1 exciton lifetime of these CNDs largely extends the collision time between T_1 state excitons and O_2 and prolongs the energy transfer time, which not only ensures a higher quantum yield of singlet oxygen (1O_2), but also facilitates the photodynamic antibacterial and anticancer effects of CNDs (Fig. 1).

Experimental

Instruments and methods

A JEM-2100 TEM (JEOL, Japan) was applied to characterize the morphological structure of CNDs. XPS was conducted on a Vario EL cube XRP spectrometer (Bruker, Germany). A Cary Eclipse fluorescence spectrophotometer (Agilent Technologies, US) was applied to record the phosphorescence and phosphorescence lifetime. For the detection of ultraviolet-visible (UV-vis) spectra, a UV-1800PC spectrophotometer (Shanghai Meipuda Instrument Co., Ltd, China) was used. 1H NMR and ^{13}C NMR were performed on an AVANCE III HD600 MHz NMR analyzer (Bruker, Germany). Infra-red spectra were recorded using a Varian 660 FT-IR spectrometer (Varian Co. Ltd, USA). The cell experiments were conducted using an MCO-15AC CO_2 thermostatic incubator (SANYO), an ECLIPSE Ts2 inverted microscope (Nikon), a CytoFLEX flow cytometer (BECKMAN), and a Flexstation® 3 enzyme labelling meter (Molecular Devices (MD)).

Materials

Triethylenetetramine hexaacetic acid (TTHA) was provided by Aladdin (USA, 98%). 3-(4,5-Dimethylthiazol-2-yl)-2,5-

diphenyltetrazolium bromide (MTT) was produced by BioFrox. Dulbecco's modified Eagle's medium (DMEM) was bought from GIBCO. Cell ROS testing kits were bought from Shanghai Beyotime Biotech Co., Ltd (China). Beef extracts and peptone were provided by Tianjin Guangfu Fine Chemicals Institute (China). Agar powder was purchased from Beijing Abxing Biotech Co., Ltd (China). Balb/c nude mice were bought from SPF Beijing Biotechnology Co., Ltd (China), and the quality testing unit was Suzhou Xishan Biotechnology Co., Ltd (China). All animal procedures were performed in accordance with the Chinese national standard (GB/T 35892-2018), which is the laboratory animal-guideline for ethical review of animal welfare, and the administrative measures for experimental animals of Shanxi Normal University. The experiments were approved by the Ethics Committee of Linfen Central Hospital, China. Other reagents (analytically pure) and kits were provided by Shanghai Sangon Biotech (China). Ultrapure water (with a resistivity equal to or more than 18.25 MΩ cm) for the experiments was produced by a Labconco ultrapure water machine (USA).

Preparation method of CNDs

Triethylenetetramine hexaacetic acid (TTHA, 0.8 g) and 30 mL of ultrapure water were added to a reaction kettle, and stirred well to dissolve. Then the kettle was transferred to a 50 mL autoclave, heated to 180 °C and maintained for 5 h. After that, the autoclave was removed and cooled to room temperature, forming a light yellow water solution. The solution was filtered through membranes (0.22 μm) and dialyzed using dialysis membranes (molecular weight cutoff was MWCO: 1000) for 48 h. Ultrapure water was changed every 4 h to remove the unreacted raw materials. Finally, the CND water solution in the dialysis membrane was collected and freeze-dried to form white solid products.

CNDs and Cy3.5 biological conjugation

Firstly, Cy3.5 (10 mg) was dissolved into 1 mL of water to form a 10 mg mL⁻¹ Cy3.5 water solution, and stored at 4 °C. Then, 2 mg of EDC, 5 mg of CNDs and 1 mg of NHS were dissolved into 0.5 mL of PBS (10 mM, pH 7.4), which was mixed at room temperature for 30 min to ensure the complete activation of the surface carboxyl groups of the QDs. In order to ensure the complete dissolution of unreacted EDC, 0.5 mL of MC Cy3.5 solution was added to the resulting solution, mixed at room



temperature for 2 h, and protected from light overnight at 4 °C. The resulting CNDs-Cy3.5 nanocomposites were centrifuged *via* ultrafiltration membranes to remove the unreacted Cy3.5, and then dissolved in 1 mL of 10 mM PBS (10 mM, pH 7.4).

Detection of cell $^1\text{O}_2$

Cell recovery. Cells (culture medium: DMEM + 10% FBS + 1% penicillin-streptomycin solution) were taken out from liquid nitrogen, and immediately put into a water bath at 37 °C. The frozen tubes were shaken gently to dissolve. After dissolution, the cells were transferred to centrifuge tubes containing 5 mL of culture medium each. After centrifugation, the cells were collected for centrifugation at the speed of 1000 rpm for 5 min at room temperature. Then the cells were suspended in a complete medium including 10% fetal bovine serum after the supernate was discarded, and finally inoculated in culture dishes. The mixtures were gently beaten and mixed, and cultured at 37 °C and 5% CO_2 saturated humidity.

Cell subculture. When the cell density reached 80%, the cells were subcultured. First, the culture medium was discarded, and PBS was used to wash the remaining part. Then the cells were digested by the addition of 1–2 mL of 0.25% trypsin and observed microscopically. After 1–2 min of digestion, the cells were found to mutually depart and become round, indicating the end of digestion. The trypsin was rapidly abandoned. Subsequently, a complete medium was added, and cells were beaten, to form a unicellular suspension. The cells were subcultured at a ratio of 1 : 3, and the expanded culture was conducted at 37 °C and 5% CO_2 saturated humidity.

Cell processing. HeLa cells at the logarithmic phase and under favorable growing status were collected, and incubated in 6-well plates (density: 5×10^5 cells per well). A blank group was set, and the cells were cultured overnight at 37 °C. Cells were grouped as follows: blank group, 200 $\mu\text{g mL}^{-1}$ CNDs + no irradiation group, and 200 $\mu\text{g mL}^{-1}$ CNDs + irradiation group (365 nm LED 15 W). After incubation for 4 h and irradiation for 30 min, the cells were further cultured for 24 h.

$^1\text{O}_2$ detection in adhering cells. A working solution was prepared by diluting DCFH-DA with a medium free of serum at the ratio of 1 : 1000. Then the cell culture medium was taken out, and the working solution was added for the incubation in an incubator at 37 °C for 20 min. After that, the cells were cleaned with a medium free of serum three times, and then the medium free of serum was added for detection and photographing under microscopy.

$^1\text{O}_2$ detection by flow cytometry. The cells were digested with 0.25% trypsin. After the digestion ended, the cells were collected, centrifuged at 1000 rpm for 5 minutes, and suspended in PBS again after the removal of the supernate, and the procedure was repeated twice. $^1\text{O}_2$ was detected by using a DCFH-DA cell ROS kit according to the manual: PBS was discarded, and diluted DCFH-DA (1 mL) was added. Cells were incubated in an incubator at 37 °C for 20 min. The whole solutions were mixed once every 3 min. Finally, the cells were washed with medium free of serum three times, and detected on a flow cytometer.

Cytotoxicity experiments

Cell recovery. Cells were removed from liquid nitrogen, and promptly put into a water bath at 37 °C. The frozen tubes were shaken gently to dissolve. After dissolution, the cells were transferred to centrifuge tubes with 5 mL of culture medium each. After centrifugation, the cells were collected for centrifugation at a speed of 1000 rpm for 5 minutes at room temperature. Then the cells were suspended in a complete medium with 10% fetal bovine serum after the supernate was discarded, and subsequently inoculated into culture dishes. The mixtures were gently beaten and mixed, and cultured at 37 °C and 5% CO_2 saturated humidity.

Cell subculture. When the cell density reached 80%, the cells were subcultured: the culture medium was discarded, and PBS was used to wash the remaining part. After the addition of 1–2 mL of 0.25% trypsin, the cells were digested and observed microscopically. After 1–2 min of digestion, the cells were found to mutually depart and become round, indicating the end of digestion. The trypsin was rapidly abandoned. A complete medium was added, and cells were beaten to form a unicellular suspension. The cells were subcultured at a ratio of 1 : 3. The expanded culture was conducted at 37 °C and 5% CO_2 saturated humidity.

Cell processing. Cells at the logarithmic phase and under favorable growing status were collected, and incubated in 6-well plates (density: 5×10^5 cells per well). A blank group was set. The cells were cultured overnight at 37 °C. The cells were processed as follows: cells were cultured with 200 $\mu\text{g mL}^{-1}$ CNDs, and either with or without irradiation (under 365 nm LED, 30 min), and then the cells were changed to a drug-free fresh culture medium for another 24 h of culture. Cells were grouped as follows: a negative control group, CND (0, 20, 200, 2000, 5000, 10 000 $\mu\text{g mL}^{-1}$) groups, action time: 0, 1, 5, 10, 30, 60 min.

MTT detection. After culturing for a certain time, 10 μL of MTT was added to each well, followed by culturing at 37 °C for 4 h. Then the culture medium was sucked out, followed by the addition of 150 μL of DMSO under vibration for 10 min. Then, an enzyme labeling meter was applied to measure the optical density at 568 nm of each well.

Procedures for animal experiments

Imaging *in vivo*. Female 6 to 8 week-old Balb/c nude mice (weighing 18–22 g) were selected and adaptively fed for 7 days. Five mice were randomly captured and tied, with the abdomens upward. Each mouse was hypodermically injected under the right arm with 200 μL of a HeLa cell suspension (containing 2×10^6 cells). After that, the mice were put back into the cages for normal feeding. When tumors grew to 70 mm^3 , the mice were intravenously injected with CNDs (amino-group Cy3.5 marked) in the tails, and the injection volume was 200 μL (200 $\mu\text{g mL}^{-1}$). Imaging *in vivo* was conducted at nine time points after the injection (0, 0.5, 1, 2, 4, 8, 16, 24, 48 h).

Measurement of blood biochemical and liver/kidney function indices. Ten mice were randomly selected and divided into 2 groups. All mice were intravenously injected with corresponding drugs: one group with PBS, and the other group with



CNDs. The injection volume was 200 μL (200 $\mu\text{g mL}^{-1}$). After that, the mice were put back into the cages for normal feeding. On day 1 and day 7 after the injection, blood was collected for measurement of biochemical indices (white blood cells WBC, red blood cells RBC, hemoglobin HGB, platelets PLT) and liver and kidney function indices (aspartic transaminase AST, alanine aminotransferase ALT, blood urea nitrogen BUN, creatinine CRE).

Anti-tumor experiments. Ten mice were randomly selected and divided into 2 groups (5 mice each). Each mouse was hypodermically injected under the right arm with 200 μL of a cell suspension (containing 2×10^6 cells). After that the mice were

put back into the cages for normal feeding. When tumors grew to 70 mm^3 , all mice were intravenously injected with corresponding drugs: one group with PBS, and the other with CNDs. The injection volume was 200 μL (200 $\mu\text{g mL}^{-1}$). After that, the mice were put back into the cages for normal feeding. 24 h after injection, the mice in one group were exposed to irradiation under a 365 nm LED lamp for 30 min, and the other group was not irradiated. After that, the mice were kept under the illumination rhythm (12 h illumination, 12 h darkness). The major diameter a and minor diameter b of each tumor were measured every other day, and the tumor volume was calculated according to the following formula: $V = ab^2/2$. During the volume

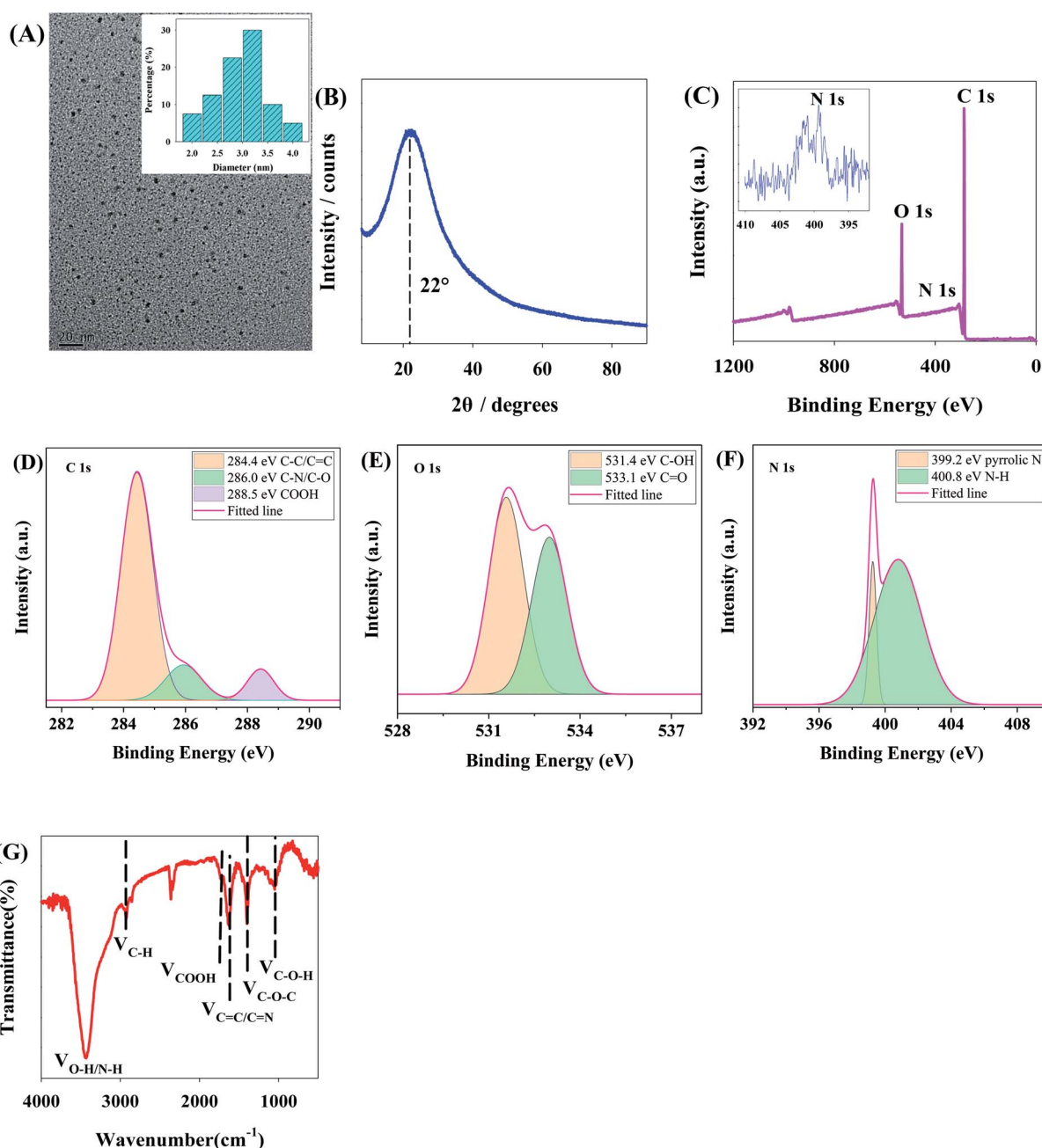


Fig. 2 Characterization of CNDs: (A) TEM image of CNDs (inset: particle size distribution); (B) XRD pattern of CNDs; (C) XPS spectrum of CNDs; (D) C 1s, (E) O 1s and (F) N 1s high-resolution spectra; (G) infrared spectrum of CNDs.



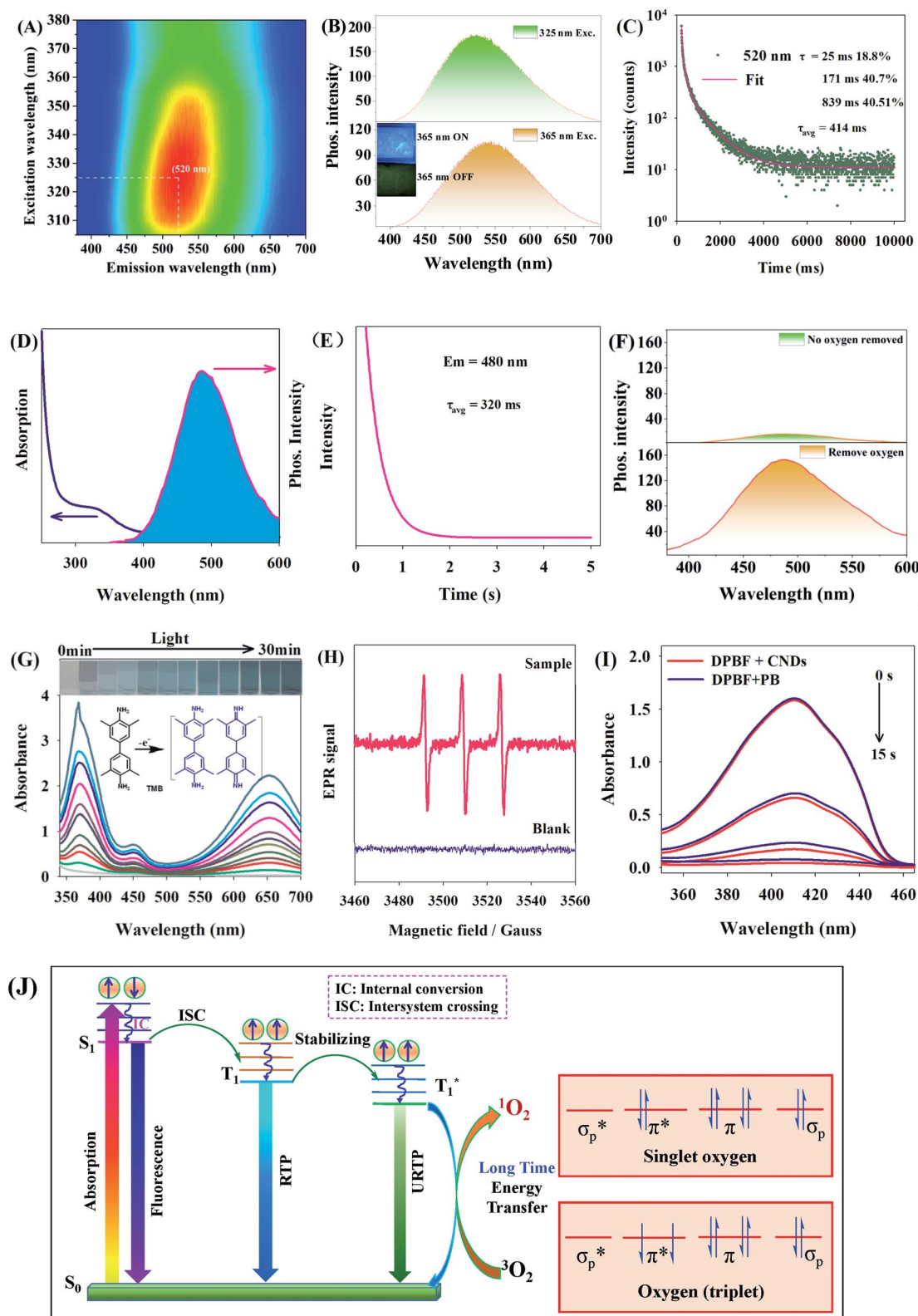


Fig. 3 URTP spectral properties of CNDs. (A) 3D URTP spectrum of CNDs; (B) URTP spectra of CNDs under excitation at 325 and 365 nm (inset: irradiation photos when a 365 nm light source is opened or closed); (C) URTP lifetime of CNDs; (D) UV absorption and URTP emission spectra of CNDs in aqueous solution; (E) URTP lifetime of CNDs in aqueous solution; (F) the URTP intensity of CNDs in aqueous solution changed under non-deoxygenating (top) and deoxygenating (bottom) conditions; (G) absorption spectrum of TMB under irradiation with ultraviolet light with CNDs (10 mg mL^{-1}) and time; (H) EPR spectrum of CNDs in the presence of TEMP (TEMP is a special spin trap for $^1\text{O}_2$, irradiation time with a 365 nm LED = 60 s, 10 mg mL^{-1} CNDs); (I) effects of CNDs and PB on UV-vis spectra of DPBF under excitation at 365 nm; (J) fluorescence and phosphorescence of CNDs, and energy transfer from O_2 to $^1\text{O}_2$.



measurement, corresponding tumor growth conditions were photographed. After 16 days, the mice were executed by cutting off the heads, and put into the relevant background single color in the corresponding group, and photographed. The tumors were taken out and put under the relevant background single color, and photographed. The heart, liver, spleen, lung, kidney and tumor tissues of each mouse were taken out through dissection and fixed separately in 4% paraformaldehyde solutions, followed by the measurement of changes in the tissues.

Results and discussion

Characterization of CNDs

Transmission electron microscopy (TEM) shows the average grain size of CNDs, 3.1 nm or so, without evident lattice fringes (Fig. 2A), indicating that these CNDs may be polymer carbon dots. X-ray diffraction (XRD) demonstrates the peak for CNDs at 22° (Fig. 2B), which is considered to indicate partial ordering inside the carbon-dots from the covalent crosslinking skeleton formed from polymerization.²⁵ This result further verifies that the CNDs are polymer carbon dots and confirms the results of TEM.

Fourier transform infrared spectroscopy (FT-IR) and X-ray photoelectron spectroscopy (XPS) were adopted to observe the surface chemical structures of CNDs. XPS shows that the CNDs are mainly composed of carbon, nitrogen and oxygen, corresponding to three characteristic peaks at 285.1 eV (C 1s), 399.1 eV (N 1s) and 532.1 eV (O 1s) respectively (Fig. 2C). Particularly, the C 1s high-resolution spectrum (Fig. 2D) is split into three characteristic peaks at 284.4, 286.0 and 288.5 eV, which are respectively ascribed to C-C/C=C, C-N/C-O and COOH. Corresponding to C-OH and C=O, the high-resolution O 1s spectrum (Fig. 2E) is divided into peaks at 531.4 and 533.1 eV. The high-resolution N 1s spectrum (Fig. 2F) is divided into peaks at 399.2 and 400.8 eV, which are attributed to pyrrolic N and N-H respectively. Besides, the surface functional groups of CNDs were further analyzed by FT-IR (Fig. 2G). The absorption peaks at 3441.2, 2945.39, 1729, 1634.3, 1410 and 1058 cm^{-1} respectively reflect the existence of O-H/N-H, and stretching vibrations of C-H, C=O, C=C/C=N, C-O-C and C-OH. It can be seen from the above XPS and FT-IR images that CNDs are rich in groups containing oxygen and nitrogen on the surface, which promote the protonation and deprotonation of CNDs.⁹

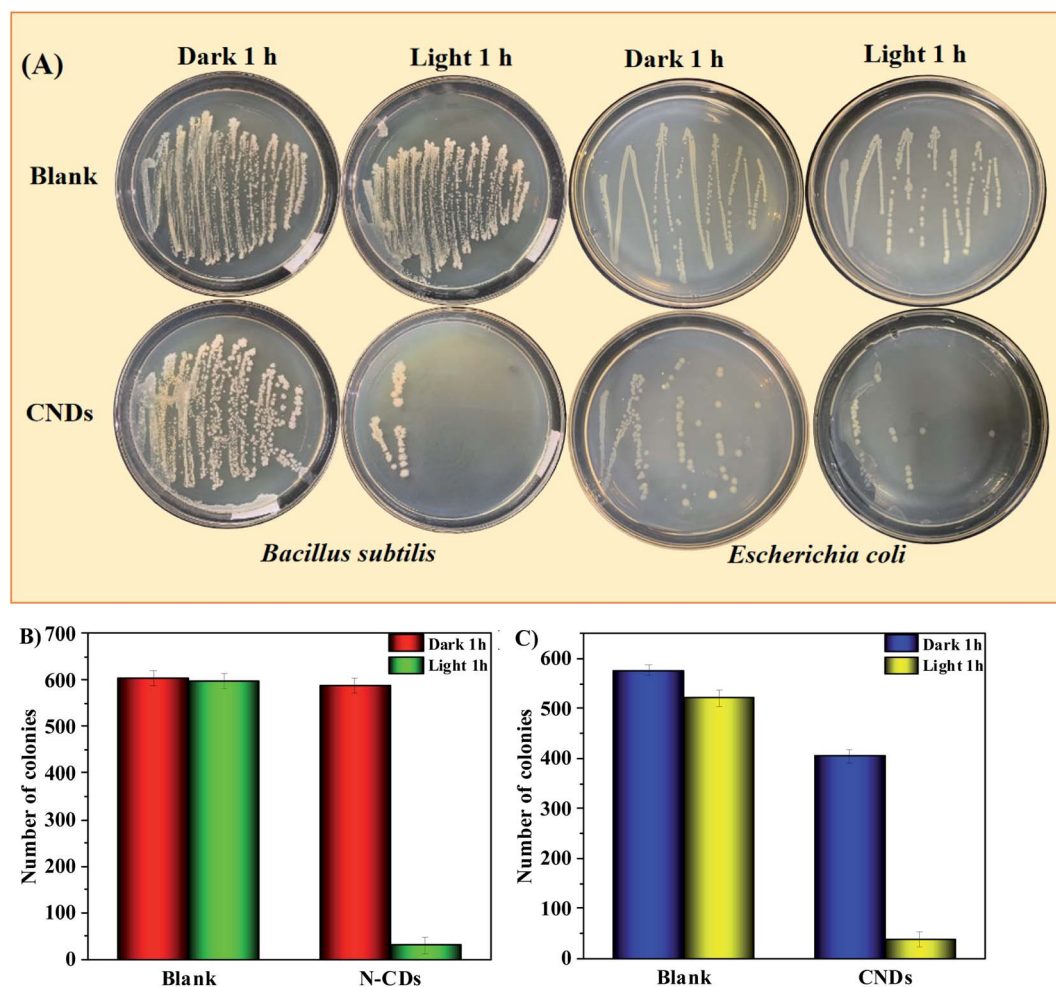


Fig. 4 (A) The effect of different concentrations of CNDs (0 and $5 \mu\text{g mL}^{-1}$) on bacteria under light/non-light conditions; the number (estimate) of colonies under different conditions: (B) *Bacillus subtilis* and (C) *Escherichia coli*.



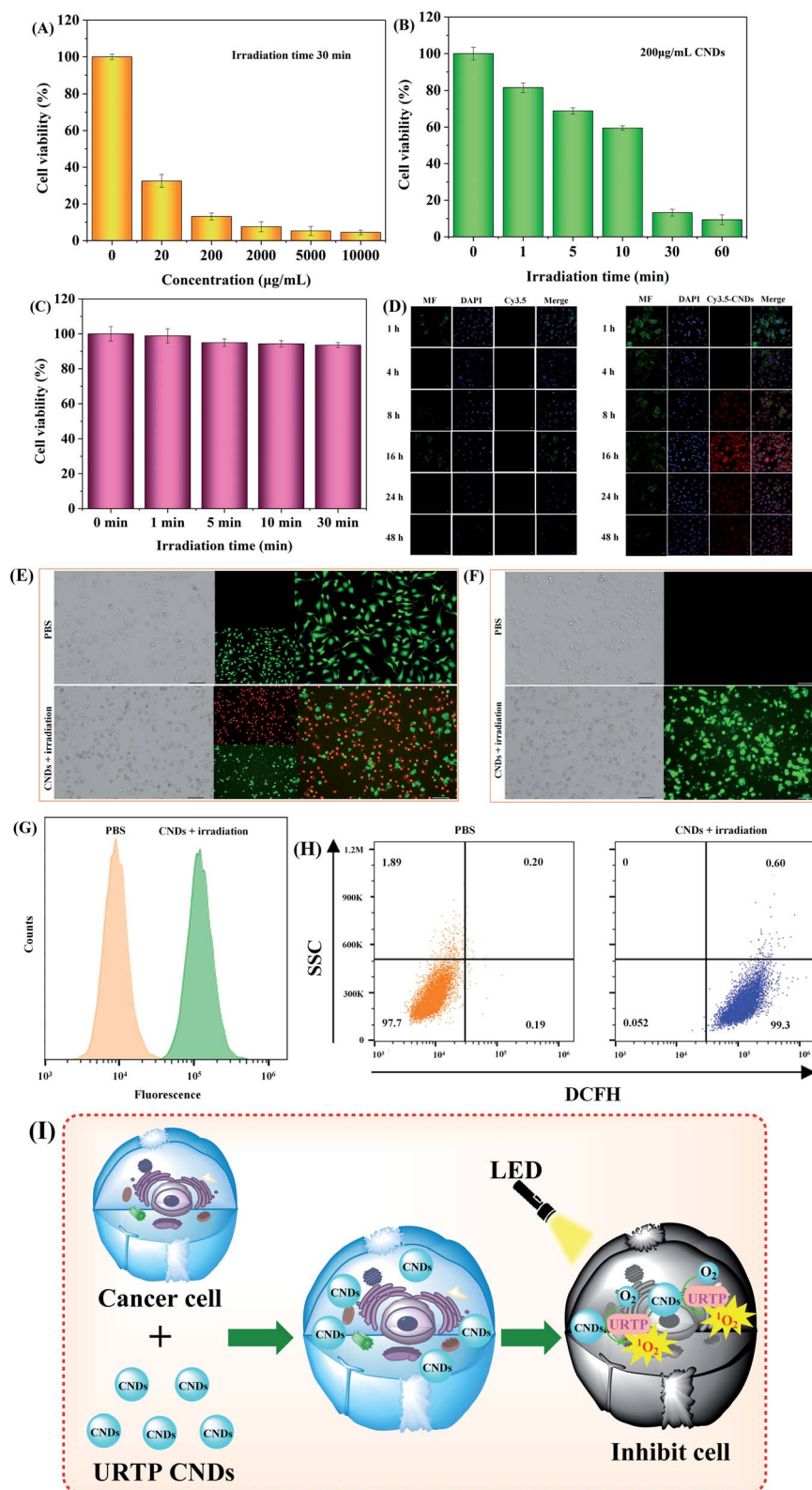


Fig. 5 Effects of CNDs on the activity of HeLa cells *in vitro*: measurement by the MTT method. (A) Effects of CND concentration (0, 2, 200, 2000, 5000, 10 000 $\mu\text{g mL}^{-1}$) on the activity of HeLa cells (30 min of irradiation); (B) effects of irradiation time (0, 1, 5, 10, 30, 60 min) on the activity of HeLa cells (CND concentration = 200 $\mu\text{g mL}^{-1}$); (C) effects of irradiation time (0, 1, 5, 10, 30 min) alone (without CNDs) on the activity of HeLa cells; (D) laser confocal microscopic images of HeLa cells incubated with (left) Cy3.5 or (right) Cy3.5-CNDs for 1, 4, 8, 16, 24, and 48 h, cell microfilaments (MF) dyed with phalloidin (green), nuclei dyed with DAPI (blue), scale at 20 μm ; (E) calcein-AM/PI staining images after processing with PBS (phosphate buffer solution) and CNDs + irradiation, dead cells (red), living cells (green), scale = 100 μm ; (F) generation of intracellular 1O_2 after processing with DCFH-DA-marked PBS and CNDs + irradiation, scale = 100 μm ; (G) effects of PBS and CNDs + irradiation on cellular 1O_2 ; (H) effects of PBS and CNDs + irradiation on cell apoptosis (ratio of apoptotic cells %); (I) photodynamic anti-HeLa cancer cell process based on CND URTP.



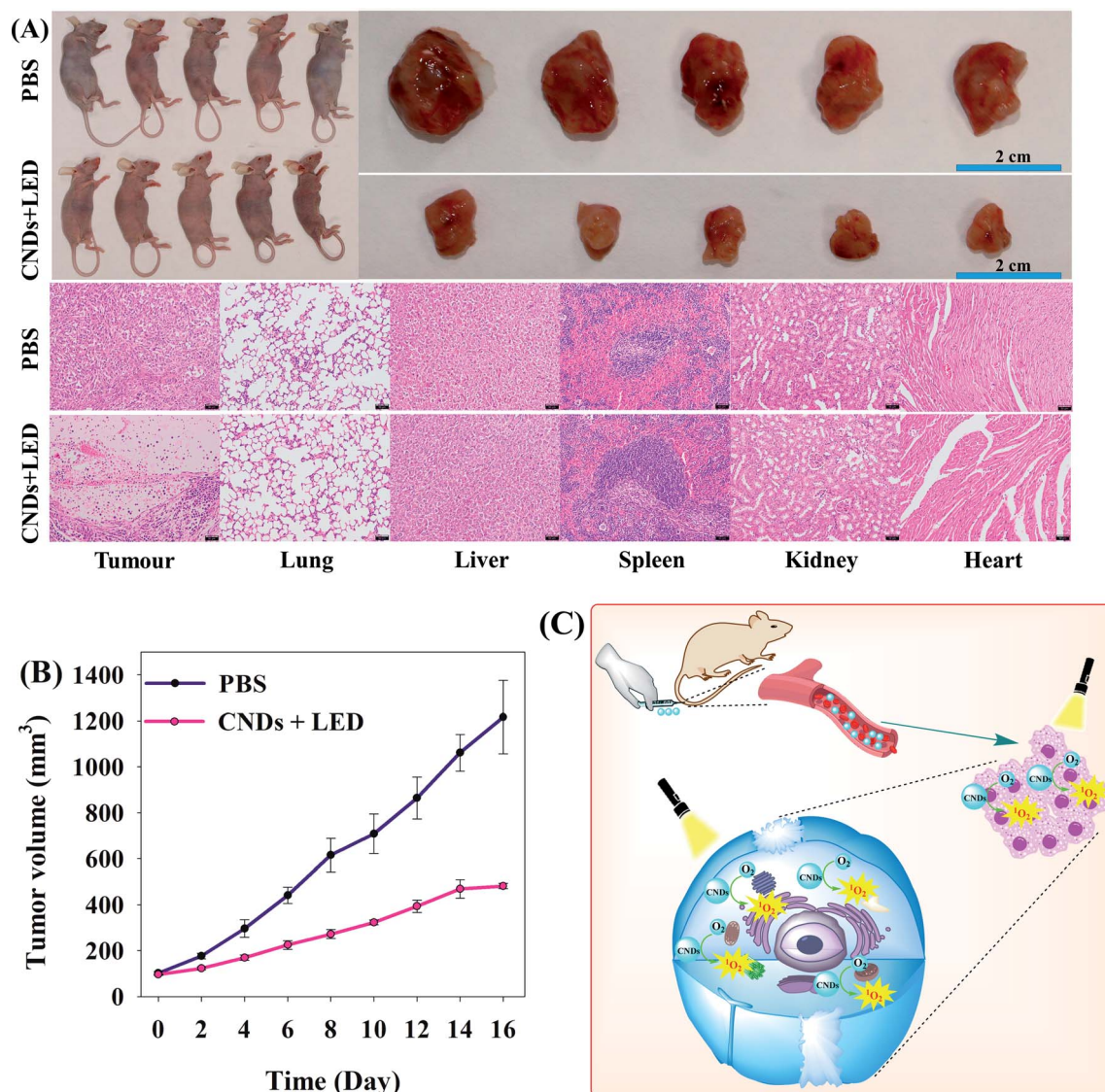


Fig. 6 Therapeutic effects of CNDs on tumors *in vivo*. (A) Images of mice and tumors at 16 days after *in vivo* tumor treatment with PBS and CNDs + LED (upper); tissue staining (H&E) in tumor, heart, liver, spleen, lung and kidney sections (lower) at 16 days after treatment of intraneous tumors with PBS or CNDs + LED, scale = 50 μ m; (B) tumor growth curves of mice after PBS or CNDs + LED treatment; (C) schematic diagram of CNDs inhibiting cancer cells.

The results above indicate that a type of polymer CND, rich in groups containing oxygen and nitrogen on the surface, has been synthesized here. Moreover, the crosslinking polymerization among groups of CNDs can effectively restrict the vibration of functional groups and inhibit the nonradiative transition of CNDs, which contributes to improving the photon yields of CNDs.

URTP properties of CNDs

In the 3D URTP spectrum of CNDs (Fig. 3A), the powder CNDs show excitation-dependent URTP, and the optimal excitation and emission wavelengths are 325 and 520 nm respectively (Fig. 3B). The powder CNDs under an LED (365 nm) emit blue fluorescence suggesting that, after the closure of the LED, green URTP can be observed by the naked eye (Fig. 3B), and the URTP average lifetime is up to 414 ms (Fig. 3C).

Fig. 3D–F show the URTP properties of CNDs in water. It can be seen from Fig. 3D that the best absorption peak of CNDs in aqueous solution is at 330 nm, the best emission peak of URTP is at 480 nm, and the average lifetime of URTP is 320 ms (Fig. 3E). When nitrogen is not supplied, the URTP of CNDs in oxygenated aqueous solution is very weak (Fig. 3F, top). However, when most O_2 is removed by nitrogen, the URTP of CNDs in aqueous solution is significantly enhanced (Fig. 3F, bottom), indicating that O_2 has a great influence on URTP.

Further observation shows that, under irradiation by a 365 nm LED light source, CNDs can gradually oxidize 3,3',5,5'-tetramethylbenzidine (TMB) (0–30 min) to give a blue colour (Fig. 3G). Under solar radiation, the unobvious change of absorption peak and color of TMB (Fig. S2†) suggests that the CND solution system efficiently generates oxides under



irradiation at a specific wavelength (365 nm). With the application of 2,2,6,6-tetramethylpiperidine (TEMP) as a singlet oxygen ($^1\text{O}_2$) trapping agent, the EPR spectrum of CNDs was measured (Fig. 3H). Results show that there are very obvious EPR signals, validating that the CND solution system under excitation at 365 nm generated $^1\text{O}_2$, which further oxidized TMB and changed its color. To further study the $^1\text{O}_2$ generating ability of CND solutions, with the application of 1,3-diphenylisobenzofuran (DPBF) as a $^1\text{O}_2$ trapping agent and photosensitizer phloxine B (PB) as a control (quantum yield = 0.65),²⁶ we calculated the $^1\text{O}_2$ quantum yield of CNDs to be 0.63 (within 15 s), suggesting that CNDs have efficient $^1\text{O}_2$ quantum yield (Fig. 3I).

Since photocatalytic energy transfer of RTP photosensitizers is achieved through intermolecular collision, the probability of collision with O_2 molecules and energy transfer is improved for CNDs with longer T_1 exciton lifetime (longer RTP lifetime), and the $^1\text{O}_2$ quantum yield is larger. Hence, the URTP of CNDs contributes to improving $^1\text{O}_2$ yields (Fig. 3J).^{13,14} In all, the cause of the high $^1\text{O}_2$ yields of CNDs is attributed to the URTP of CNDs (lifetime of long-lifetime T_1^* excitons).

Doping with nitrogen atoms can fundamentally affect the electronic structure of carbon atoms,^{27–31} so appropriate doping with nitrogen can effectively promote the spin-orbit coupling (SOC) and intersystem crossing (ISC) between the excited singlet and triplet states of CNDs, and increase the quantum yields of T_1 -state excitons of CNDs. More importantly, the CNDs in this study are a type of polymer CND; due to the covalent crosslinking frame structure of polymers, CNDs can form a relatively stable rigid environment, which inhibits the non-radiative attenuation of triplet excitons in CNDs, stabilizing the triplet state excitons, but also prolonging the RTP lifetime. It is this covalent crosslinking frame structure that endows CNDs with URTP in water solutions. The obvious long-lifetime observed in the solid state is caused by the fact that the abundant surface functional groups ($-\text{OH}$, $-\text{COOH}$) provide many sites for the formation of hydrogen bonds between surface CNDs and inner CNDs. Moreover, the dense hydrogen bond skeletons between surface sites and inner sites can isolate O_2 (Fig. S2†), thereby preventing URTP from being quenched. To validate the presence of hydrogen bond skeletons, we analyzed the differential scanning calorimetry (DSC) of solid CNDs (Fig. S3†). The results show that severe endothermic changes occurred within 50–90 °C, proving the existence of hydrogen bond skeletons in CNDs.

Inhibitory effect of CNDs on bacteria

Fig. 4 shows the action of CNDs (0 and 5 $\mu\text{g mL}^{-1}$) against a Gram-positive bacterium (*Bacillus subtilis*) and a Gram-negative bacterium (*Escherichia coli*) with or without a 365 nm LED. Clearly, under the condition of CNDs + 365 nm LED, the counts of bacterial plaques in both species are far smaller than that of the system without CNDs or without illumination (Fig. 4A), and the antibacterial rates against *B. subtilis* and *E. coli* are up to 94% and 93% respectively (Fig. 4B and C). Hence, under an excitation source at 365 nm, CNDs can convert O_2 to

$^1\text{O}_2$ via URTP photocatalytic oxidation, and thereby promote the killing effects on both *B. subtilis* and *E. coli*.

Inhibition effect of CNDs on HeLa cells *in vitro*

Regarding the $^1\text{O}_2$ generating ability of CNDs, we studied the photodynamic therapy (PDT) ability of CNDs on HeLa cells *in vitro*. The cytotoxicity at different concentrations of CNDs (0, 20, 200, 2000, 5000, 10 000 $\mu\text{g mL}^{-1}$) and varying irradiation time (0, 1, 5, 10, 30, 60 min) was measured by a standard MTT method (Fig. S4A–S4F†). With the absence of irradiation, CND concentrations $\leq 200 \mu\text{g mL}^{-1}$ nearly did not affect the cell survival rate (Fig. S4A†), indicating that CNDs under a certain concentration show high biocompatibility. However, when CND concentration $\geq 200 \mu\text{g mL}^{-1}$ (Fig. 5A) and irradiation time ≥ 30 min (Fig. 5B), the cell survival rates were smaller than 15%. With the absence of CNDs, irradiation times ≤ 30 min almost did not affect cell survival rate (Fig. 5C). In all, 200 $\mu\text{g mL}^{-1}$ CNDs and irradiation time of 30 min were selected as the optimal PDT conditions for HeLa cells.

To investigate the behaviors of CNDs in HeLa cells *in vitro*, amido Cy3.5 ($\text{Ex}_{576}/\text{Em}_{604}$)-marked CNDs were selected, so that CNDs were more easily observed under laser confocal microscopy. The HeLa cells incubated with free Cy3.5 only displayed slight red fluorescence from 1 to 16 hours (left in Fig. 5D), but the red fluorescence of the Cy3.5/CNDs group (right in Fig. 5D) was significantly stronger. These results indicate that the HeLa cells can well ingest Cy3.5/CNDs, and the fluorescence intensity of cells incubated with Cy3.5/CNDs weakens after 16 hours, which may be caused by Cy3.5/CNDs being discharged out of the cells by cell metabolism.

Under irradiation by a 365 nm LED, HeLa cells were processed with PBS or 200 $\mu\text{g mL}^{-1}$ CNDs, and then stained with propidium iodide (calcein-AM/PI) and calcein-AM, which respectively visualized dead cells (red) and living cells (green) (Fig. 5E). The results showed that CNDs + LED lead to massive death of HeLa cells. Moreover, the generation of intracellular $^1\text{O}_2$ was detected by means of a fluorescent dye (2',7'-dichlorodihydrofluorescein diacetate (DCFH-DA)) that could infiltrate cells and react with $^1\text{O}_2$ to emit green fluorescence. The results show that abundant $^1\text{O}_2$ is formed in HeLa cells (Fig. 5F), which is the direct cause of massive death of HeLa cells. Besides, apoptosis analysis (Fig. 5G and H) demonstrated that HeLa cells under CNDs + LED irradiation produced abundant $^1\text{O}_2$, which subjected 99.9% of HeLa cells to apoptosis. The above results suggest that the toxicity of CNDs to HeLa cells can be caused by the intracellular $^1\text{O}_2$ produced by CNDs under 365 nm LED irradiation; CNDs as URTP photosensitizers will convert O_2 to $^1\text{O}_2$, produce intracellular $^1\text{O}_2$, and then inhibit HeLa cell proliferation (Fig. 5I).

PDT of intraneous cancers by CNDs

To determine the time dependence of CND distribution in mice *in vivo*, we recorded the time-dependent fluorescence imaging of mice. The results showed that between 24 and 48 h after the injection of CNDs/Cy3.5, CNDs/Cy3.5 was obviously accumulated in the tumor parts (Fig. S5†).

To further investigate the PDT effect of CNDs on tumors *in vivo*, we studied the anti-tumor effect *in vivo* on Balb/c nude mice carrying HeLa tumors. When the HeLa tumor volume reached about 70 mm³, 10 mice were divided into a PBS group and a CNDs + LED group (since CNDs alone or LED irradiation alone nearly did not affect HeLa cells under our experimental conditions, we did not set a CND group or an LED group, for the sake of maximally protecting animals). The treated mice were intravenously injected with 200 μ L of 200 μ g mL⁻¹ PBS or CNDs, and 24 h later, the CND treated mice were irradiated by a 365 nm LED (15 W) for 30 min. During the following 16 days, tumor volumes were monitored (Fig. 6A and B). The results showed that tumors in the CNDs + LED group and PBS group were significantly inhibited. Hematoxylin & eosin (H&E) staining suggested (lower part in Fig. 6A) that the tumor tissues in the CNDs + LED group were significantly necrotic, but the tumor tissues were normally shaped in the PBS group; other tissues (heart, liver, spleen, lung, kidney) were not obviously injured, indicating that the CNDs + LED treatment did not cause any severe side effects. Moreover, we also studied the toxicity *in vivo* of intravenous PBS and CNDs (200 μ L, 200 μ g mL⁻¹) on Balb/c nude mice. The results indicated that liver and kidney function indices (AST, ALT, BUN, CRE) or blood biochemical indices (WBC, RBC, HGB, PLT) of the PBS group and CND group were all within normal ranges after 1 day or 7 days (Fig. S6 and S7[†]), showing no significant differences ($P > 0.05$). Thus it can be seen from the above results that CNDs have both favorable therapeutic effects on cancers and safety.

In all, the rationale for cancer treatment with CND PDT is that: CNDs injected into Balb/c nude mice are transported by the blood system to tumor sites. Under 365 nm LED irradiation, the CNDs generate ultralong-lifetime triplet state (T_1^*) excitons, and the energy transfer between the T_1^* excitons and O₂ (the ground state is the triplet state) produces more highly-oxidizing ¹O₂, leading to non-specific oxidative damage to biomolecules (lipids, proteins, nucleic acids) on cell membranes or in cells and finally inhibiting tumor growth (Fig. 6C).

Conclusions

A one-step hydrothermal method was applied to synthesize URTP CNDs, which showed URTP under solid conditions and more importantly, in a water environment. The URTP of CNDs in water solutions largely prolongs the collision time between T_1 excitons and O₂, as well as the energy transfer time, improving the quantum yield of ¹O₂, and thus realizing the photodynamic antibacterial and anticancer applications of CNDs. Featuring eco-friendliness, low cost and high biocompatibility, CNDs are ideal photodynamic antibacterial and anticancer nanomaterials.

Author contributions

Conceptualization: Yanming Miao, Xinhao Zhang, Jinyao Li and Jinzhi Lv; formal analysis: Yanming Miao, Xinhao Zhang, Jinyao Li, Wenli Yang, Xiaomin Huang and Jinzhi Lv; funding acquisition: Yanming Miao and Jinzhi Lv; methodology: Yanming Miao, Jinyao Li, Wenli Yang, Xiaomin Huang and Jinzhi Lv;

writing – original draft: Yanming Miao, Xinhao Zhang, Jinyao Li and Wenli Yang; writing – review & editing: Xiaomin Huang and Jinzhi Lv.

Conflicts of interest

There are no conflicts to declare.

Acknowledgements

The work was completed with the support of the National Natural Science Foundation of China (NSFC) (Grant 32171393, 31700862 and 32001202).

References

- 1 F. Cieplik, D. Deng, W. Crielaard, W. Buchalla and E. Hellwig, *Crit. Rev. Microbiol.*, 2018, **44**, 571–589.
- 2 X. Dong, W. Liang, M. J. Mezziani, Y. P. Sun and L. Yang, *Theranostics*, 2020, **10**, 671–686.
- 3 D. Wang, L. Niu, Z. Y. Qiao, D. B. Cheng, J. Wang, Y. Zhong, F. Bai, H. Wang and H. Fan, *ACS Nano*, 2018, **12**, 3796–3803.
- 4 J. Wang, Y. Zhong, X. Wang, W. Yang, F. Bai, B. Zhang, L. Alarid, K. Bian and H. Fan, *Nano Lett.*, 2017, **17**, 6916–6921.
- 5 J. Ge, M. Lan, B. Zhou, W. Liu, L. Guo, H. Wang, Q. Jia, G. Niu, X. Huang, H. Zhou, X. Meng, P. Wang, C. S. Lee, W. Zhang and X. Han, *Nat. Commun.*, 2014, **5**, 4596.
- 6 H. Wang, X. Yang, W. Shao, S. Chen, J. Xie, X. Zhang, J. Wang and Y. J. Xie, *J. Am. Chem. Soc.*, 2015, **137**, 11376–11382.
- 7 Z. Zhou, Y. Zhang, Y. Shen, S. Liu and Y. Zhang, *Chem. Soc. Rev.*, 2018, **47**, 2298–2321.
- 8 X. Zheng, L. Wang, Q. Pei, S. He, S. Liu and Z. Xie, *Chem. Mater.*, 2017, **29**, 2374–2381.
- 9 J. Zhang, X. Lu, D. Tang, S. Wu, X. Hou, J. Liu and P. Wu, *ACS Appl. Mater. Interfaces*, 2018, **10**, 40808–40814.
- 10 Y. Miao, S. Liu, L. Ma, W. Yang, J. Li and J. Lv, *Anal. Chem.*, 2021, **93**, 4075–4083.
- 11 S. Han, G. Lian, X. Zeng, Z. Cao, Q. Wang, D. Cui and C. P. Wong, *Nano Res.*, 2020, **13**, 3261–3267.
- 12 R. Knoblauch, A. Harvey, E. Ra, K. M. Greenberg, J. Lau, E. Hawkins and C. D. Geddes, *Nanoscale*, 2021, **13**, 85–99.
- 13 R. Gao, X. Mei, D. Yan, R. Liang and M. Wei, *Nat. Commun.*, 2018, **9**, 2798.
- 14 L. Xu, K. Zhou, H. Ma, A. Lv, D. Pei, G. Li, Y. Zhang, Z. An, A. Li and G. He, *ACS Appl. Mater. Interfaces*, 2020, **12**, 18385–18394.
- 15 F. Wang, Y. H. Chen, C. Y. Liu and D. G. Ma, *Chem. Commun.*, 2011, **47**, 3502–3504.
- 16 H. Jia, Z. Wang, T. Yuan, F. Yuan, X. Li, Y. Li, Z. Tan, L. Fan and S. Yang, *Adv. Sci.*, 2019, **6**, 1900397.
- 17 V. D. Dang, A. B. Ganganboina and R. A. Doong, *ACS Appl. Mater. Interfaces*, 2020, **12**, 32247–32258.
- 18 H. Lu, C. Li, H. Wang, X. Wang and S. Xu, *ACS Omega*, 2019, **4**, 21500–21508.
- 19 L. Zhang, Y. Yang, M. A. Ziaee, K. Lu and R. Wang, *ACS Appl. Mater. Interfaces*, 2018, **10**, 9460–9467.



- 20 K. M. Tripathi, H. T. Ahn, M. Chung, X. A. Le, D. Saini, A. Bhati, S. K. Sonkar, M. I. Kim and T. Kim, *ACS Biomater. Sci. Eng.*, 2020, **6**, 5527–5537.
- 21 Z. Ye, G. Li, J. Lei, M. Liu, Y. Jin and B. Li, *ACS Appl. Bio Mater.*, 2020, **3**, 7095–7102.
- 22 H. Yan, B. Zhang, Y. Zhang, R. Su, P. Li and W. Su, *ACS Appl. Bio Mater.*, 2021, **4**, 6703–6718.
- 23 P. Long, Y. Feng, C. Cao, Y. Li, J. Han, S. Li, C. Peng, Z. Li and W. Feng, *Adv. Funct. Mater.*, 2018, **28**, 1800791.
- 24 Y. Gao, H. Zhang, S. Shuang and C. Dong, *Adv. Opt. Mater.*, 2020, **8**, 1901557.
- 25 J. H. Zhu, M. M. Li, S. P. Liu, Z. F. Liu, Y. F. Li and X. Li. Hu, *Sens. Actuators, B*, 2015, **219**, 261–267.
- 26 B. Zhao and Z. A. Tan, *Adv. Sci.*, 2021, **8**, 2001977.
- 27 Y. Sun, S. Liu, L. Sun, S. Wu, G. Hu, X. Pang, A. T. Smith, C. Hu, S. Zeng, W. Wang, Y. Liu and M. Zheng, *Nat. Commun.*, 2020, **11**, 5591.
- 28 S. A. Shaik, S. Sengupta, R. S. Varma, M. B. Gawande and A. Goswami, *ACS Sustainable Chem. Eng.*, 2021, **9**, 3–49.
- 29 K. Holá, M. Sudolská, S. Kalytchuk, D. Nachtigallová, A. L. Rogach, M. Otyepka and R. Zbořil, *ACS Nano*, 2017, **11**, 12402–12410.
- 30 S. Wu, R. Zhou, H. Chen, J. Zhang and P. Wu, *Nanoscale*, 2020, **12**, 5543–5553.
- 31 M. Sudolská and M. Otyepka, *Appl. Mater. Today*, 2017, **7**, 190–200.

